Lattice Gas Automata for Simple and Complex Fluids

Shiyi Chen,[1,2] **G. D. Doolen,**[2] **and W. H. Matthaeus**[1]

We review some recent applications of lattice gas automata, including flow through porous media, phase transitions, thermodydrodynamics, and magnetohydrodynamics.

KEY WORDS: Lattice gas; flow through porous media; phase transition; thermohydrodynamics; magnetohydrodynamics.

1. INTRODUCTION

The recent development of lattice gas automata[33–35,64] has provided a new numerical method for solving the Navier–Stokes equations and other partial differential equations. Lattice gas automata are idealized many-body systems that allow particles to move and scatter in a discretized lattice space at discrete times. The basic idea in a lattice gas is to use simple microscopic operations on a lattice to generate meaningful statistical macroscopic quantities, which could be either the solution of partial differential equations or some other interesting physical phenomena.

The most important property of lattice gas models from the point of view of particle motions and collisions is that all operations are purely discrete, local, and logical which is ideal for parallel computing. A speed of $3 * 10^8$ cell updates per second on a CRAY-XMP and $8 * 10^9$ cell updates per second on a Connection-Machine 2 can be obtained. A fundamental feature of the lattice gas model is its flexibility. The original simple lattice gas model can be generalized to simulate many different physical systems. At the present stage, lattice gas methods can solve many partial differential equations, including the Navier–Stokes equations,[25,29,41,42,46,51,77,82] the Burgers equation,[5,23] the Poission

---

equation,[17] the wave equation,[15,49] and the diffusion equation[2,4,54,68]; and model many physical phenomena, including flow through porous media,[1,7,19,72,80] turbulent flows,[57,81] phase transitions,[12–14,18] multiphase flows,[9,21,43,47,73,78] chemical-reacting flows,[27,55,76] thermohydrodynamics,[10,20,24,63] magnetohydrodynamics,[16,65] liquid crystals,[18,59] and semiconductors.[70] Lattice gas methods locally conserve total mass, momentum, and energy exactly during all processes. Thus, there is no roundoff error and the scheme is unconditionally stable. Moreover, lattice gas methods can easily handle very complicated geometry and boundary conditions. For example, the nonslip condition can be implemented by particle velocity reversal at boundaries, which is crucial for its applications in flow through porous media. Theoretical studies of lattice gas systems are also relatively simpler than classical continuum systems. Transport properties[26,40,48,52,58,83] and long-time behavior of correlations[38,39] can often be exactly solved, while they are more difficult to obtain in continuum systems.

There are two main restrictions for lattice gas models in the simulation of fluid flow. First, the Reynolds numbers and Mach numbers cannot be too big. The incompressible Navier–Stokes equations are obtained only in the low-Mach-number limit.[60] This restriction can be relaxed if one uses multiple discrete velocity models.[8,11] Second, signals in lattice gas models are usually noisy,[28,22] requiring spatial and time averaging. Lattice Boltzmann methods,[61] in which real numbers replace the bits in the lattice gas model, greatly reduce the fluctuations. In the present paper, we intend neither to discuss methods to overcome the problems in lattice gases[63,20] nor to give general conclusions for the validation of these models nor to compare the lattice gas techniques with traditional methods. We restrict ourselves to the basic principles of the lattice gas methods, introduce some detailed lattice gas models that have been developed, and discuss their applications.

The paper is organized as follows: In Section 2, we present the basic ideas of the lattice gas and discuss the two- and three-dimensional lattice gas models, which form the basis of all other models. Section 3 discusses single-phase and two-phase flow through porous media, which have emerged as an important application of lattice gas methods during the last 4 years. In Section 4, we will discuss a phase transition model, which can be used to simulate shock waves and to model liquid crystal hydrodynamics. Section 5 describes the temperature-dependent lattice gas model, including Bénard convection. Section 6 discusses our recent developments on magnetohydrodynamics, including the simulation results of classical Hartman flow and Alfvén waves. In the last section, we give a brief summary on the current and future research on this field.

2. BASIC PRINCIPLES OF LATTICE GAS METHODS

Unlike the lattice Boltzmann method[61] and discrete velocity models,[8,11] lattice gas methods emphasize the discreteness and use only very few values of velocity. Lattice gas methods for hydrodynamic systems were originally proposed by Hardy *et al.* (HPP)[44,45] on a square lattice in two dimensions. But there are serious problems in the square lattice, notably spurious momentum conservation and nonisotropy of the stress tensor. The important contribution made by Frisch *et al.* (FHP)[41] was to show that a hexagonal lattice gas model has an isotropic stress tensor and has greatly reduced the spuriously conserved quantities.

The basic 2D six-bit FHP lattice gas model[41,82] consists of identical particles on a hexagonal lattice with lattice unit $c = 1$. All particles have the same mass and they reside only on the sites of the hexagonal lattice. There are six different particle momentum states at each lattice site, associated with the directions $\mathbf{e}_a = [\cos(2\pi a/6), \sin(2\pi a/6)]$, $a = 1,..., 6$. An exclusion rule is imposed so that no more than one particle at a given site can have a given momentum state. If we use $N_a(\mathbf{x})$, $a = 1,..., 6$, to denote the particle occupation in state a at site $\mathbf{x}$, then $N_a = 0$ or 1. There are two microscopic updating processes at each discrete time step: advection and collision. In the advection process, a particle in state $\mathbf{e}_a$ moves from its present site to the nearest neighbor site in the direction $\mathbf{e}_a$; all particles have the same speed ($= 1$) and the same kinetic energy. In the collision process, particles at each site are redistributed among the six momentum states at the same site in such a way that the total particle number ($= \sum_{a=1}^{6} N_a$) and the total momentum ($= \sum_{a=1}^{6} \hat{e}_a N_a$) are conserved. Since all particles have the same mass and speed, energy conservation is equivalent to mass conservation for this model. The original FHP model only uses two-body and three-body collisions. In order to decrease viscosity and increase the Reynolds number Re ($Re = UL/\nu$, U and L are the characteristic velocity and length of the system, respectively; ν is the kinematic viscosity), the saturated collision[30] has been used. In addition to that, one can also add another bit to represent a particle at rest, greatly increasing the collision frequency and the Reynolds number. It can be shown that at equilibrium the FHP lattice gas behaves like an ideal gas,[42,82] $p = n/2$, where n is the average particle density and the sound speed is $1/\sqrt{2}$.

The microdynamical evolution of the FHP system can be described exactly by the following microscopic equation:

$$N_a(\mathbf{x} + \mathbf{e}_a, t + 1) = N_a(\mathbf{x}, t) + \Lambda_a \tag{1}$$

where Λ_a represents the collision operator, which includes the creation or

annihilation of a particle in momentum state e_a and only depends on the information at the site x at time t. The collision operation has the form

$$A_a = \sum_{s,s'} (s' - s) \, P(s \to s') \prod_j N_j^{s_j} (1 - N_j^{s_j})^{1-s_j} \qquad (2)$$

where $s = (s_1, s_2, ..., s_6)$ and s' represent the local states before and after collision. $P(s \to s')$ is the transition probability from state s to s'.

Particle and momentum conservation are satisfied if $\sum_{a=1}^{6} A_a = 0$ and $\sum_{a=1}^{6} e_a A_a = 0$. The fluid density and momentum are defined as follows:

$$n(\mathbf{x}, t) = \sum_a f_a(\mathbf{x}, t)$$

$$\mathbf{j}(\mathbf{x}, t) = n\mathbf{v} = \sum_a f_a(\mathbf{x}, t)\mathbf{e}_a \qquad (3)$$

where

$$f_a(\mathbf{x}, t) = \langle N_a(\mathbf{x}, t) \rangle$$

and $\langle \cdots \rangle$ denotes an ensemble average.

If the microscopic collision transition probability P in (2) satisfies the semi-detailed balance condition

$$\sum_s P(s \to s') = 0$$

then one can prove that collisions will make the system approach a local equilibrium, described by a Fermi–Dirac distribution:

$$f_a = \frac{1}{1 + \exp(\alpha + \beta \mathbf{e}_a \cdot \mathbf{v})} \qquad (4)$$

where α and β are Lagrange multipliers determined by mass and momentum conservation.

Assuming $L \gg 1$ and $T \gg 1$, where T is the macroscopic characteristic time, from (1), one obtains the continuum version of the kinetic equation:

$$\partial_t f_\alpha + \mathbf{e}_a \cdot \nabla f_a = \Omega_a \qquad (5)$$

where Ω is the collision operation obtaining by replacing f_a for N_a in A. After ensemble averaging the microscopic equation and using the Chapman–Enskog expansion, it can be shown that the FHP system approximates the following fluid equations[41,42]:

$$\partial_t n + \nabla \cdot (n\mathbf{v}) = 0$$

$$\partial_t(n\mathbf{v} + \nabla \cdot [ng(n)\mathbf{v}\mathbf{v}] = -\nabla p + \nu \nabla^2 (n\mathbf{v}) \qquad (6)$$

$$p = \tfrac{1}{2}[n - g(n)\mathbf{v}^2]$$

where $g(n) = (n-3)/(n-6)$ for the six-bit model. The density dependence of $g(n)$ causes a non-Galilean effect. The incompressible Navier–Stokes equations are recovered only in the low-Mach-number limit when time, pressure, and viscosity are rescaled by the factor g for constant-density problems.

The four-dimensional face-centered-hypercubic lattice (FCHC) was proposed by d'Humières *et al.*[31] to simulate three-dimensional problems.[19,71] The four-dimensional model was chosen because no three-dimensional single-speed lattice model yields and isotropic stress tensor to fourth order in the velocity. The FCHC lattice is the set of all points on the integral lattice for which the sum of the coordinates is even. Each lattice site has 24 nearest neighbors that are a distance $\sqrt{2}$ away. Particle collisions in each site can involve up to 24 particles and conserve mass and momentum. The velocity of a particle at site x can be defined as e_a, $a = 1, 2,..., 24$. A periodic condition for the fourth dimension is used, leading to the pseudo-FCHC model. Projecting the physical quantities to three-dimensional space, one obtains fluid equation (6) with $g(n) = 2(24 - 2n)/3(24 - n)$.

3. A LATTICE GAS APPLICATION: FLOWS THROUGH POROUS MEDIA

One of the most successful applications of the lattice gas methods is the flow through porous media.[1,19,72] Here the Reynolds numbers are small and flow geometry is very complicated, a major difficulty for the traditional method. Nonslip and free-slip conditions can be implemented easily by chosing the velocity reversal and symmetry relection at the boundary.

Darcy's law plays an essential role in flow through porous media. It relates the flow flux and the pressure drop across a complex sandstone slab:

$$q = -\frac{K}{v}\frac{dp}{dx} \tag{7}$$

where q is the volume flow rate per unit area, dp/dx is the pressure gradient, and K is the permeability. The permeability only depends upon pore structure. It is independent of the fluid transport coefficients for low-Reynolds-number flows. Determination of permeability is the one of main objectives for research on flow through porous media.

Using lattice gas simulations, we have studied the relationship between permeability and porosity and fractal dimension of the sandstones. Media

can be generated with a prescribed porosity and fractal dimension.[19] For all calculations, we use a nonslip condition at solid boundaries. In Fig. 1, we present a typical velocity vector field for two-dimensional lattice gas simulations. The pressure difference between the edges of the left and right is 0.2. By measuring the flux through sandstone for a given pressure difference, one can calculate the permeability of the sandstone using (7). In Figs. 2a and 2b, we present the numerical results of the measurements of permeability as a function of porosity ε and fractal dimension of the sandstone D. The calculated permeabilities agree qualitatively with realistic observations.[32]

In Fig. 3, we show the pressure distribution in real sandstone (1024×600 lattice cells). The geometry is the digitized image of an etched glass micromodel. Dark blue represents the medium and the other colors represent pressures. In Fig. 4, we show the spatially averaged (in y direction) pressure as a function of x. One can see a qualitative agreement with
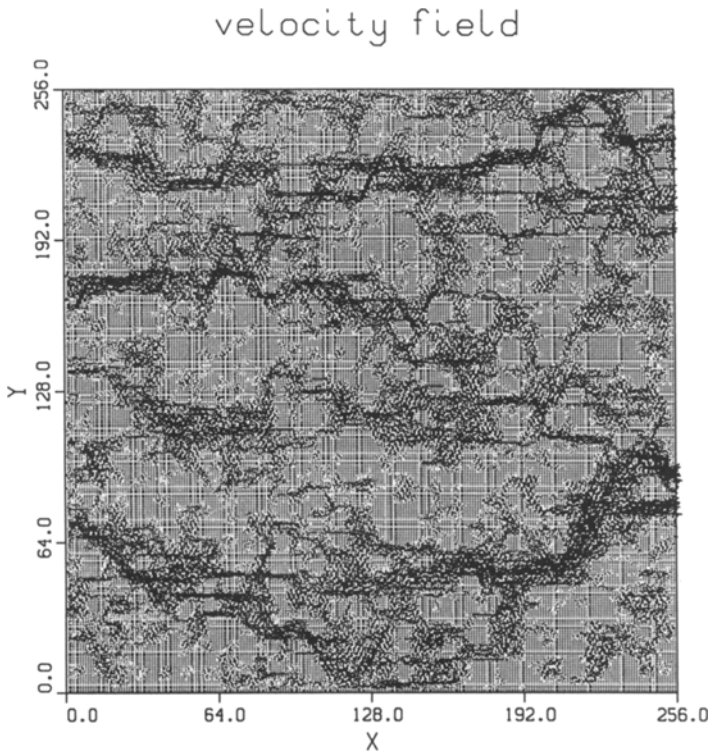

Fig. 1. A typical velocity distribution for flow through porous media in a complicated boundary.

a linear pressure drop across the sample except near the inlet and outlet regions. The direct experimental measurement of the permeability for this micromodel is approximately 23 darcys. Our lattice gas simulation yielded 21.9 darcys. Simulation and experiment agree within 5%.

Two-phase immiscible fluids can be simulated by an extension of the original FHP-type lattice gas model. The important property to model two-phase flows is the surface tension between the fluids and the wettability between fluid and solid materials. In order to represent two different fluids, such as gas and liquid, Rothman and Keller[73,74] first introduced the concept of colored particles. In their model, different types of particles are painted with different colors to represent different fluids. In order to model short-range attractive interactions between particles of the same type, a local color gradient was used in the local collision rules, which required the nearest-neighbor color information. They successfully applied this model to several physical problems, including the calculation of relative permeability, viscous fingering, and phase spinodal decomposition. Somers and Rem[78] introduced a different lattice gas model for two-phase flows. Their idea is to use the colored holes to store information of the local particle colors. The important contribution of this colored hole picture is to make the collision rules purely local. This made the implementation more efficient than earlier models. Recently, we have extended Somers and Rem's model to viscous fingering, surface tension, and contact angles between
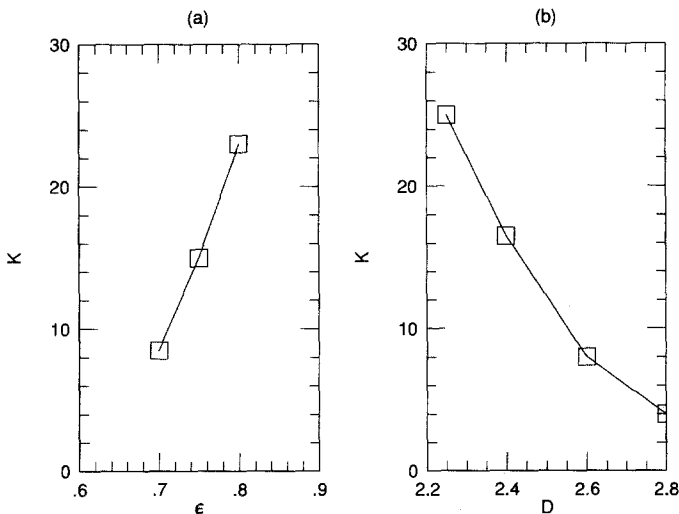

Fig. 2. (a) The permeability versus porosity for fractal dimension $D = 2.5$. (b) The permeability versus the fractal dimension of sandstone for porosity $\varepsilon = 0.7$.

Fig. 3. Pressure distribution for flow through porous media. The dark blue represents the sandstone, the left side (red) is the high-pressure region. and the right side (blue) is the low-pressure region. The sandstone is digitized from a micromodel. The measurement of the permeability for this geometry is about 5% error compared with experimental measurement.

fluids and solid walls.[21] Applications of this model to physical flows have successfully shown the qualitative agreement with experiment.

In our new model, particles and holes are colored red or blue (we use black for red and white for blue in plots in this paper). As many as six moving particles and one rest particle (all with unit mass) may occupy each lattice site simultaneously. For each direction at a given site, we assign a two-bit Boolean variable $(f_i(\mathbf{x}, t), N_i(\mathbf{x}, t))$, $i = 1, 2,..., 7$, for space $\mathbf{x}$ and time t, where $(0, 0)$ represents a blue hole, $(0, 1)$ a red hole, $(1, 0)$ a blue particle, and $(1, 1)$ a red particle. This lattice gas model requires 14 bits per sit. Exclusion of particle and holes is used to allow only one particle or one hole in a given state. Particles do not change colors during advection or collision processes and holes can change colors during collision process. In order to ensure that the two-phase fluids satisfy the Navier–Stokes equations, we have to enforce mass conservation for each color particle and total momentum conservation. This procedure produces the following constraints for the collision rules:

$$\sum_i N_i f_i = \sum_i N_i' f_i'$$

$$\sum_i N_i(1 - f_i) = \sum_i N_i'(1 - f_i')$$

and

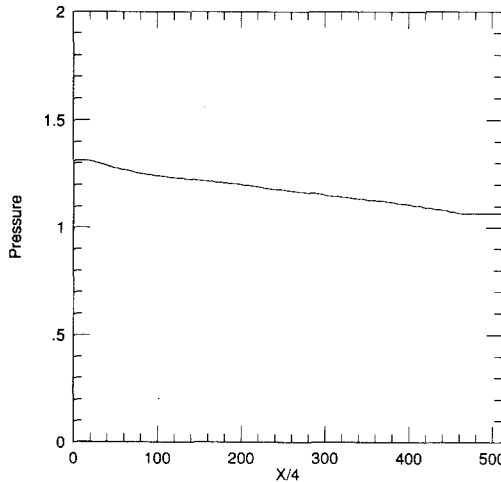$$\sum_i N_i \mathbf{e}_i = \sum_i N_i' \mathbf{e}_i \tag{8}$$

Fig. 4. Pressure distribution along the x direction after averaging in the y direction.

The essential idea in our new collision rules is to have the color holes retain the memory of particles of the same color. We let this color information propagate and influence collisions in such a way that particles scatter preferentially in the direction opposite to the same color hole. Therefore, the color hole field near a color interface plays an important role in determining the directions of colored particles after collisions. Colored holes are created and destroyed as follows. When a particle changes direction in a collision, a hole of the same color is created in the original direction. A particle annihilates any hole if one exists in the new direction. Thus, the consequence of this rule for colored holes is that information about the local particle color is transmitted by the holes a distance on the order of a mean free path.

We define the local particle color flux field **G** and hole color flux field **F** as follows:

$$\mathbf{G} = \sum_i (2f_i - 1) N_i \mathbf{e}_i$$

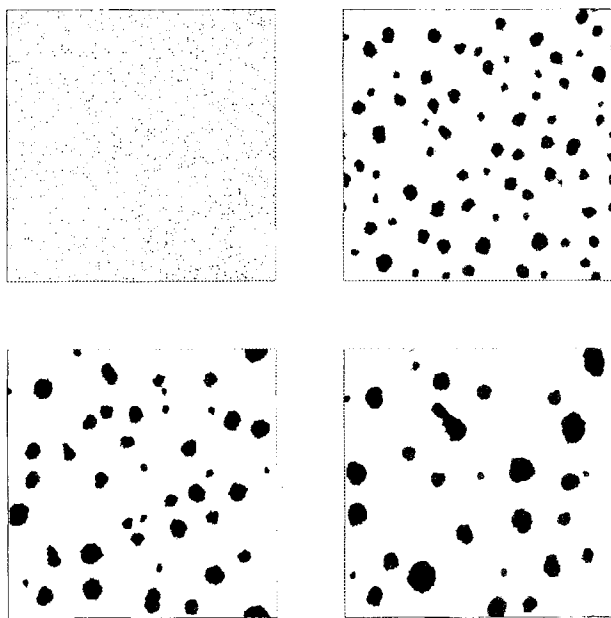$$\mathbf{F} = \sum_i (2f_i - 1)(1 - N_i) \mathbf{e}_i$$

(9)

Fig. 5. Two-phase oil and water mixture configurations in a lattice gas simulation at different times: $t = 0$, 4000, 8000, and 12000. Black represents oil drop and white represents water, with $d < 0.4$ and $d_r/d = 0.1$.

Our rules for particle collisions are as follows: First, we choose the output state from all possible output states which maximize the quantity $Q = -\mathbf{F} \cdot \mathbf{G}'$, where F is calculated from an input hole state and G' is calculated for the possible output particle states. This step forces colored particles to move in the opposite direction to the local color gradient. Second, when there are several configurations that have the same maximum value of Q, then we choose the output having the minimum $|G'|$. This step directs the colored particles as closely as possible in the opposite direction of the local color hole flux. The third step is to preferentially produce output states with a rest particle. This slows down the flow of the fluid and enhances phase separation as well as the surface tension. Fourth, if ambiguity remains, then we choose the output that minimizes the viscosity. This step requires that the output state be different from the input state. One can verify that the above operations reduce the maximum degeneracy to six. For real coding, we randomly pick one of the possible output states at each time step.

In Fig. 5, we present oil drop distributions (represented by black) in a water background (represented by white) after an initial randomly mixed state. One can see the existence of the attractive force between the same-color particles from the spinodal decomposition process.[74] The surface tension can be determined by measuring the pressure difference across the interface of the drop. Figure 6 is a typical total pressure distribution across a drop. We have also measured the surface tension, given by the Laplace
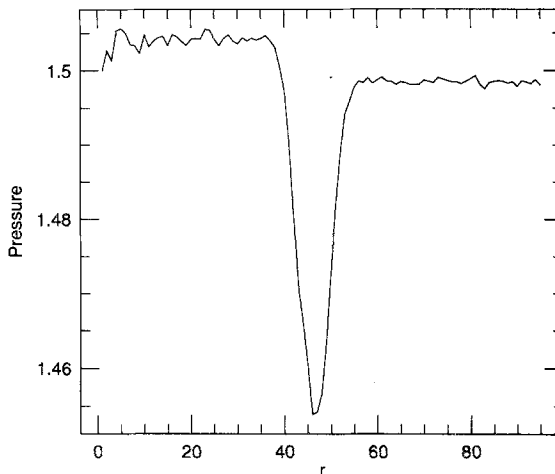

Fig. 6. Pressure distribution as a function of distance r from the center of the bubble. The pressure change at the interface demonstrates the existence of surface tension. The simulation has been done for $d = 0.4$ and $d_r/d = 0.1$.
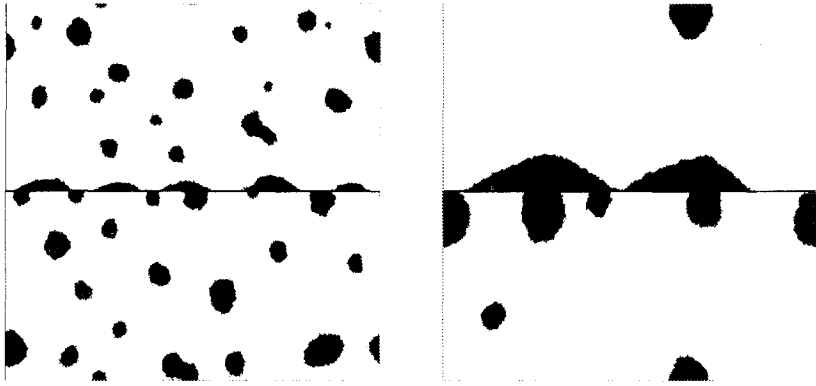
Fig. 7. Contact angle dimonstrations for $d = 0.4$ and $d_r/d = 0.1$ at $t = 1000$ and 100,000. There is a wall in the middle of space with $P_b = 0.8$ in the upper part and $P_r = 0.8$ in the lower part.

formula,[32] versus the radius for a total density $d = 0.4$ and red particle density $d_r = 0.1$. We find that the surface tension is independent of the radius.

The idea to use holes to represent the local particle color memory can be also used to create the potentials for the interaction between solid
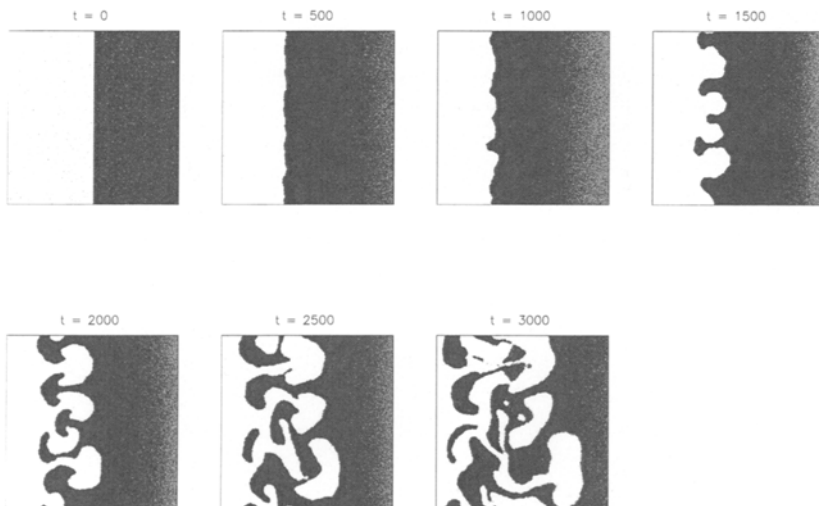

Fig. 8. Typical configurations for two-dimensional Rayleigh–Taylor instability with a denser fluid (dark black) above a less dense fluid (white) under the influence of gravity. The light black represents the cells with zero particle occupation. Times shown in the plots are in lattice units.

material and fluids. If a hole collides with a wall, it can bounce back and
change its color with probability P. The magnitude of P determines the
intensity of the attraction between the wall and the same-color particles.
A typical contact angle for red fluids is shown in Fig. 7.

In Fig. 8, we present a simulation for two-dimensional Rayleigh–
Taylor instability. The gravitational forcing is from right to left. The fluid
in dark black is denser than the fluid in white. The extra forcing for dark
black fluid is approximately 0.0048 each time step per site if there are states
allowed to be forced.[51] With the evolution of time, one sees clearly that
an instability occurs and the fingering emerges. This quanlitatively agrees
with observations[69] and other numerical simulations.[6]

4. PHASE TRANSITION

There are several possible strategies for extending the lattice gas
methods to describe phase transitions. In the work by Cécile et al.,[12,13] a
lattice gas model was developed to simulate the gas–liquid phase transition
by introducing a long-range interaction. Here, we only discuss the simplest
possible model[14] that describes a phase transition. To model phase
transition phenomena and nonideal gas equation of state with local inter-
action rules, it is important to introduce at least two energy levels in the
lattice gas model.

In addition to the traditional six-bit FHP moving particles, we use a
"bound pair" particle, which has zero momentum and twice the mass of
moving particles. The simple interactions between moving particles and
bound pairs are as follows: a head-on collision between moving particles
will be changed to be a bound-pair particle; and a bound-pair particle will
change to be two particles with zero total·momentum. This transition
process between moving particles and bound pairs follows a Markov
process. A transition probability for the system to change from one state to
another is proportional to $\exp(-\beta \Delta E)$, where ΔE is the potential energy
difference between the two states and β is the reciprocal temperature
defined for the canonical ensemble. It can be shown that the canonical
ensemble is the equilibrium invariant measure for this lattice gas system
with temperature $1/\beta$.[62] The potential energy change associated with a
binding transition at a site is $\Delta E(\mathbf{x}) = -\varepsilon_0 \sum_{i=1}^{6} N_0(\mathbf{x} + \mathbf{e}_i)$. A binding
probability $\phi = \lambda \exp(-\beta \Delta \Delta E)/[1 + \exp(-\beta \Delta E)]$ $(\lambda \leqslant 1)$ is assigned at
each site of the lattice. The unbinding probability $\bar{\phi}$ for bound pairs is
$\lambda(1 - \phi)$. A transition is not allowed if it leads to a state which has more
than one particle per microstate. For example, if $N_0 = 1$, $\bar{\phi}$ is sampled and,
if successful, one of the three paired momentum directions is chosen with

equal probability. An unbinding is allowed only if no free particles occupy the chosen pair of directions. If $N_0 = 0$, one of the three paired momentum directions is chosen with equal probability. If the chosen pair of the free particle states is occupied, ϕ is sampled and, if successful, a binding occurs such that the pair of free particles from a bound pair and N_0 becomes one. For fixed β, $\lambda = 1$ leads to the shortest time for the system to reach equilibrium. Advection and elastic collision processes also occur at each time step. The FHP model is the special case with $\beta = -\infty$.

The modified microdynamical kinetic equation becomes

$$N_a(\mathbf{x} + \mathbf{e}_a, t + 1) = N_a(\mathbf{x}, t) + \Lambda_a + \Pi_a; \qquad a = 1,..., 6$$

$$N_0(\mathbf{x}, t + 1) = N_0(\mathbf{x}, t) + \Pi_0 \tag{10}$$

where the additional term Π_a $(a = 0,..., 6)$ compared with (1) is the contribution from the transition processes:

$$\Pi_a = \mathscr{B}_a^+ (1 - N_a(\mathbf{x}, t)) - \mathscr{B}_a N_a(\mathbf{x}, t), \qquad a = 0,..., 6 \tag{11}$$

In (11), $\mathscr{B}_a^+$ and $\mathscr{B}_a$ $(= 0, \text{ or } 1)$ are the creation and annihilation operators for N_a due to the transition processes, which depend on the particle occupations at site $\mathbf{x}$ and the configuration of the bound pairs at the six nearest-neighbor sites. The detailed form of Π_a guarantees that the particle occupation for each state is either 0 or 1. From the explicit expressions for $\mathscr{B}_a$ and $\mathscr{B}_a^+$,[20] one can show that the conservation of mass and momentum requires $\sum_{a=1}^6 \Pi_a + 2\Pi_0 = 0$ and $\sum_{a=1}^6 \mathbf{e}_a \Pi_a = 0$.

To approximate the equation of state, we use a mean field approximation which assumes: (i) no correlations between particles in different states at the same site and same time,

$$\langle N_a(\mathbf{x}, t) N_b(\mathbf{x}, t) \rangle = \langle N_a(\mathbf{x}, t) \rangle \langle N_b(\mathbf{x}, t) \rangle, \qquad a \neq b$$

and (ii) homogeneous particle distributions: $\langle N_a(\mathbf{x}) \rangle = \langle N_a(\mathbf{x}') \rangle$. It can be shown using an H-theorem[42] that the equilibrium distribution for the moving particles has the same form as (4), and the rest particle distribution has the form

$$f_0 = \frac{1}{1 + \exp(2\alpha - \beta\varepsilon)} \tag{12}$$

where $f_0 = \langle N_0 \rangle$ represents bound-pair distribution. ε is the average potential energy per bound pair. Density is defined as

$$n = \sum_a f_a + 2f_0 \tag{13}$$

It can shown that this model still obeys the hydrodynamic equation (6), except for a different equation of state.

In Fig. 9, we present the mean-field results for the equation of state, using solid lines for three reciprocal temperatures ($=0.2$, 0.6, and 1.0). V is the specific volume, $1/n$. The simulation was done for zero velocity in a system with 64×64 lattice cells. Computer simulations also showed that the finite-system-size effect is negligible for such a system. The $\times$, $\diamond$, $+$, and $\square$ in Fig. 9 represent different reciprocal temperatures $\beta = 0.2$, 0.6, 1.0, and 1.2. These simulations clearly show a critical point for $1 < \beta < 1.2$ where $\partial p / \partial V = 0$. This can be proved by a method of mapping our model to a two-dimensional Ising model on a hexagonal lattice. The critical point of phase transition is $\beta = 1.09$.[18]

The sound speed in this model near the transition point can be arbitrarily small. This feature is useful for simulating high-Mach-number flows. In Fig. 10, we present simulation results for a piston problem which studies the formation of shock waves. A periodic condition is used in the y direction. We initialize the flow with uniform velocity along the x direction and place a fixed wall on the right. The sound speed for this system is 0.16 and the fluid velocity is 0.3.

The nearest-neighbor bound-pair interaction can be extended to include the interactions between particles with different orientations for
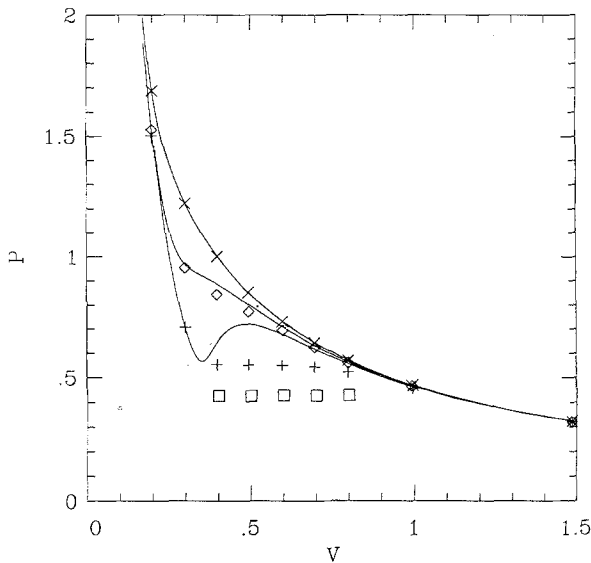

Fig. 9.   Phase diagram for a lattice gas model with phase transition. The $\times$, $\diamond$, $+$, and $\square$ represent different reciprocal temperatures $\beta = 0.2$, 0.6, 1.0, and 1.2.

simulating liquid crystals. For doing that, we allow bound-pair particles to have an orientational degree of freedom θ which is restricted to be a multiple of 60°, because of the hexagonal lattice nature. The general inter-action Hamiltonian between two particles at different sites and orientations can be represented by $H = H(\theta_{ij}, r)$. Here θ_{ij} is the relative angle between particles i and j, and r is the distance between them. In order to extend the model to liquid crystals, we restrict the Hamiltonian to be an even function of θ. Physically this restriction is related to the indistinguishability of head and tail of the macroscopic properties of liquid crystals. We have designed lattice rules which describe a transition between an orientationally ordered state and a disordered state which correspond to the nematic–isotropic transition. For simplicity, we assume that the Hamiltonian can be written as a summation of products of a function of angle and a function of distance: $H(\theta, r) = \sum_n H_n(\theta) H_n'(r)$. It has been proved[79] rigorously that no long-range order can exist in systems with such a separable potential. Further, we take $H'(r)$ to be the same as in the model we discussed earlier.
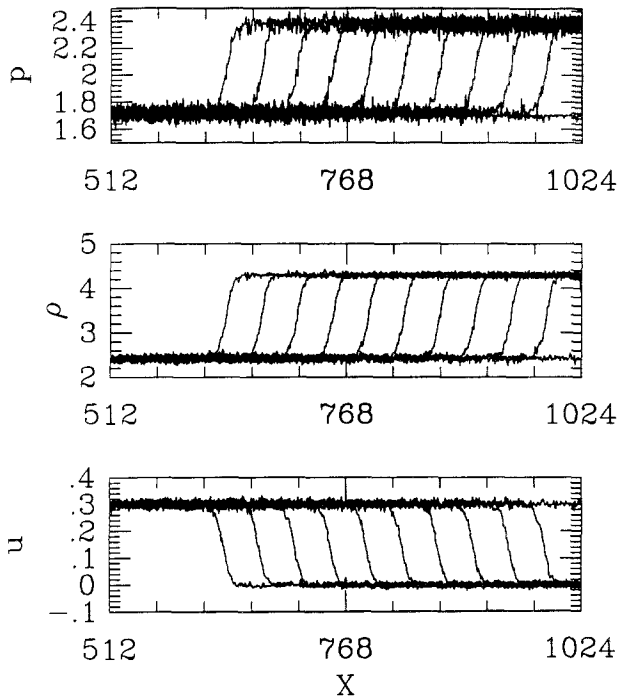

Fig. 10. Discontinuous interfaces in a shock wave simulation when Mach number is 1.875: pressure, density, and velocity profiles at different times ranging from $t = 0$ to $t = 1000$. Time interval is 100.

There are several possibilities for $H(\theta)$; for D-dimensional problems, it is interesting to study the following interaction potential:

$$H(\theta) = \frac{D \cos^2(\theta) - 1}{D - 1} \tag{14}$$

For this Hamiltonian, a randomly distributed orientation will give zero average for $\langle H(\theta) \rangle$. A completely parallel orientation will have $\langle H(\theta) \rangle = 1$. When the interactions between orientations are isotropic, it is possible to observe two-phase transitions of the Kosterlitz–Thouless type.[53] The order parameter for the system is defined as the ensemble average of $H(\theta)$. In order to test the effect of the position interaction potential $H(r)$ on $H(\theta)$, we introduce the parameter χ, the ratio of $H(r)$ to $H(\theta)$. Then $H(r, \theta)$ in $D = 2$ is

$$H(r, \theta) = \chi H(r) + 2 \cos^2(\theta) - 1 \tag{15}$$

where $H(r) = \varepsilon_0 N_0(\mathbf{x}) \sum_{i=1}^{6} N_0(\mathbf{x} + \hat{e}_i)$ and θ is the relative orientation angle between the nearest-neighbor bound pairs.

The lattice gas simulation has been done for a system with a 64×64 lattice cells. in Fig. 11, we present $\langle H(\theta) \rangle$ versus β for density $\rho = 4.8$ for $\chi = 0.05$, and 1.0, denoted by $\square$, $\times$, and $\diamond$ respectively. We see that the transition is not of the first-order type in which there would be a jump of the order parameter in the phase diagram. Rather, a continuous behavior
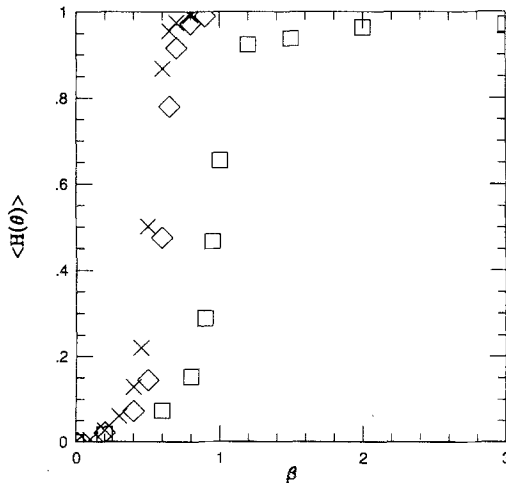
Fig. 11.   The order parameter $\langle H(\theta) \rangle$ as a function of β for $\chi = 0$. ($\square$), 0.5 ($\diamond$), and 1.0 ($\times$) for $\rho = 4.8$.
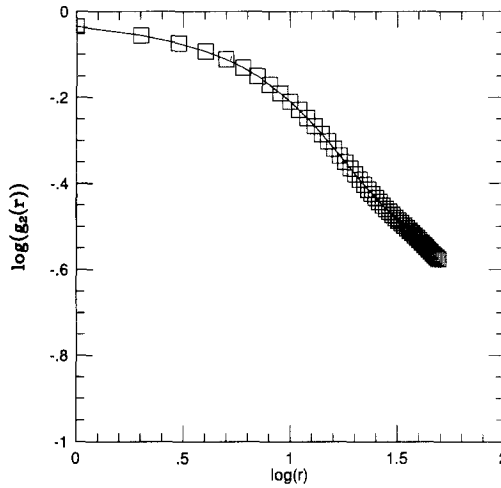
Fig. 12.   A typical correlation function $\langle \cos\{2[\theta(r)-\theta(0)]\}\rangle$ versus spatial separation. An algebraic decay is seen in the range from $r=20$ to 50.

is found, where one has a big change of the value of the order parameter over a small interval of β values.

The low-temperature ordered phase is characterized by quasi-long-range order, with a power-law decay for the correlation function $g_2(r)$ defined as follows:

$$g_2(r) = \langle \cos\{2[\theta(r)-\theta(0)]\}\rangle \tag{16}$$

where $\theta(r)-\theta(0)$ is the angular difference between an orientation at a given position and the orientation at r. A typical correlation function $g_2(r)$ versus spatial separation r is presented in Fig. 12 in log–log plot at $t=20,000$ after a random initial condition. This time integral is long enough to allow the system relax to equilibrium. We found that the spatial decay rate is not exponential, which would characterize short-range correlation. Also, we observe that for r smaller than 7, the correlation decays faster than algebraic, while for $20 \leqslant r \leqslant 50$, we observe a linear decay (an algebraic decay in the linear coordinate). This indicates a quasi-long-range order.

5. THERMOHYDRODYNAMICS

In six-bit lattice gas models,[41] energy conservation is equivalent to the mass conservation; therefore, the energy equation is not an independent equation. In seven-bit models,[30] the kinetic equation does not conserve

total particle kinetic energy, for the collision cases involved rest particles. Thus, it is useful to include at least three different particle speeds in the model in order to study temperature-dependent effects. Here we consider the simplest case: a lattice gas model with three types of particles, distinguished by their speeds and masses. Without loss of generality, we assume the particles have the speeds zero, one, and two, with masses $m_\sigma = 2/3$, 1, and 1/2, respectively. Therefore, in this model, we have 12 nonzero-velocity states and one zero-velocity rest state allowed at each lattice site: $\mathbf{e}_a^\sigma = c_\sigma[\cos(2\pi a/6), \sin(2\pi a/6)]$, $a = 1,..., 6$; $c_\sigma = 0$, 1, and 2. If ε_a^σ is the unit mass kinetic energy for type σ particles, then $\varepsilon_a^\sigma = \frac{1}{2}|\mathbf{e}_a^\sigma|^2$. Here σ ($= 0$, 1, or 2) denotes the type of particle. For each type of particle, the Fermi-exclusion rules applys.

It is important to choose the collision rules conserving not only mass and momemtum, but also energy. Then the collision operator Λ_a in (1) has the following constraint:

$$\sum_{a, \sigma} m_\sigma \Lambda_a^\sigma (\mathbf{e}_a^\sigma)^2 = 0.$$

Example of collisions are shown in Fig. 13. Usually, there are three kinds of collisions: (i) collisions between the same type of particles, (ii) collisions between different types of particles, but conserving the number of each type of particle, (iii) collisions that allow a change in the number of each type of particle, such as Fig. 13c. Only the last type of collision can change particle species. These three kinds of collisions can occur simultaneously or sequentially. For simultaneous collisions, there is no order preference for the collisions. One simply takes the entry particle configuration and redistributes particles while following the conservation rules. This usually requires a large collision table for a system with many possible particle velocities. Sequential collisions, however, will split the collision operations into an arbitrary number of steps with a subset of the collisions occuring during each step. Each collision uses the present particle distributions and requires fewer bits to describe collisions. For example, in Fig. 13, we can have the first kind of collision for speed-one and speed-two particles. Then we use the updated particles as input for the second kind of collision. Then we could use the updated particles as input for the third kind of collision. In order to simplify the collision tables, we adopt the sequential collisions for the computations.

The particle equilibrium distribution in (4) is replaced by the following equation:

$$f_a^{\sigma(0)} = \frac{1}{1 + \exp[m_\sigma(\alpha + \beta \mathbf{e}_a^\sigma \cdot \mathbf{v} + \gamma \varepsilon_a^\sigma)]}$$

due to the additional energy conservation. The second-order moment of (5) gives the energy equation

$$\frac{\partial(n\varepsilon)}{\partial t} + \nabla \cdot (n\varepsilon \mathbf{v}) + \nabla \cdot \mathbf{q} + 2\hat{P}:\nabla \mathbf{u} = 0 \tag{17}$$

where ε is the local kinetic energy defined by the formula $n\varepsilon = \sum_{a,\sigma} m_\sigma f_a^\sigma (\mathbf{e}_a^\sigma - \mathbf{v})(\mathbf{e}_a^\sigma - \mathbf{v})$, $\mathbf{q}$ is the heat flux, $(\mathbf{q})_\alpha = \sum_{a,\sigma} m_\sigma f_a^\sigma (\mathbf{e}_a^\sigma - \mathbf{v})^2 (\mathbf{e}_a^\sigma - \mathbf{v})_\alpha$, and $\hat{P}$ is the pressure tensor, $\hat{P}_{\alpha\beta} = \sum_{a,\sigma} m_\sigma f_a^\sigma (\mathbf{e}_a^\sigma - \mathbf{v})_\alpha (\mathbf{e}_a^\sigma - \mathbf{v})_\beta$. With the standard procedure of expansion for small velocity, for models in which the rest particle does not have internal
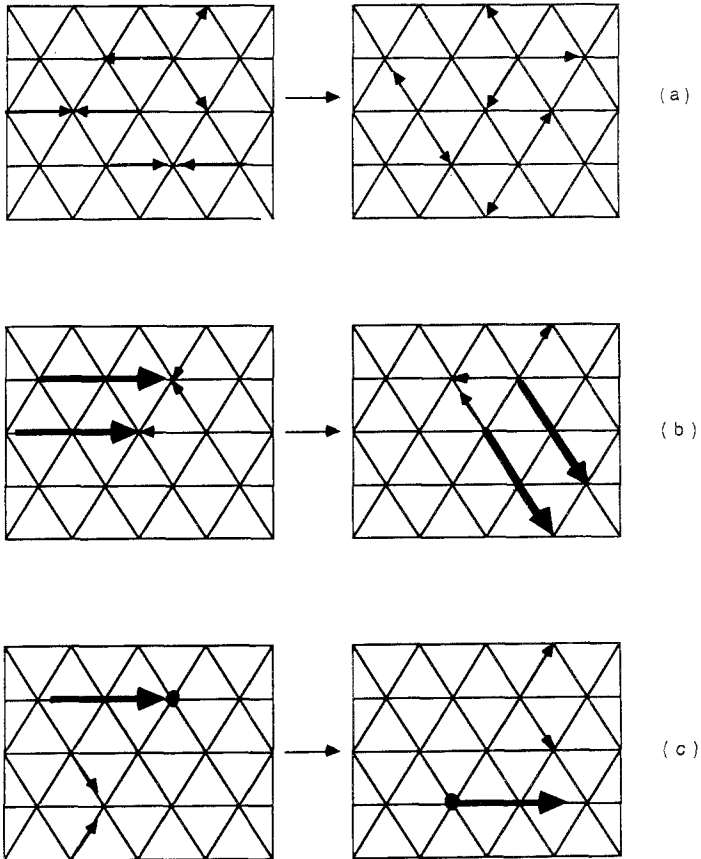

Fig. 13. Some typical collision rules in the lattice gas model with temperature variable. Note that the mass is different for different particles, and the collisions conserve the total mass, momentum, and energy.

energy, we have the stress tensor $\hat{\Pi}_{\alpha\beta} = \sum_{a,\sigma} m_\sigma f_a^\sigma (\mathbf{e}_a^\sigma)_\alpha (\mathbf{e}_a^\sigma)_\beta$ in the first order as follows:

$$\hat{\Pi}_{\alpha\beta}^{(0)} = ng(n, \varepsilon) u_\alpha u_\beta + p\delta_{\alpha\beta}$$

where $\delta_{\alpha\beta}$ is the Kronecker symbol, $g(n, \varepsilon)$ is the coefficient of the convective term,

$$g(n, \varepsilon) = \frac{\beta_0^2 M}{D(D+2)n} \sum_\sigma m^{\sigma 3} d_\sigma (1 - d_\sigma)(1 - 2d_\sigma)|c^\sigma|^4 \tag{18}$$

and

$$p = p_0 + p_1 u^2$$

In the above equations, M is the number of distinct velocity directions (six for a hexagonal lattice), D is the space dimension (two for our model), d_σ and c_σ are the particle density and velocity for each direction for σ-particles, and β_0 is the zeroth-order expansion of β.

The equation of state can be written as follows:

$$p_0 = \sum_\sigma m_\sigma d_\sigma |c^\sigma|^2 \frac{M}{D} = n\varepsilon \tag{19}$$

and

$$p_1 = \frac{n}{2} [1 - g(n, \varepsilon)]$$

Note that Eq. (19) indicates that the equation of state for this lattice gas system is that of an ideal gas.

To order u^3, the heat flux vector $q_i^{(0)}$ is

$$q_i^{(0)} = h(n, \varepsilon) + \chi u^2 u_i + n\varepsilon u_i \tag{20}$$

where

$$h(n, \varepsilon) = \frac{D}{2M} \frac{n \sum_\sigma m_\sigma d_\sigma (1 - d_\sigma)|c^\sigma|^4}{(\sum_\sigma m_\sigma d_\sigma (1 - d_\sigma)|c^\sigma|^2)(\sum_\sigma m_\sigma d_\sigma c_\sigma^2)} - 2$$

and χ is a complicated function depending on the detailed structure of the lattic e gas model.[20] The complete equations for momentum and energy up to $O(u^2)$ have the form

$$\partial_t(n\mathbf{v}) + \nabla \cdot (ng(n, \varepsilon) \mathbf{v}\mathbf{v}) = -\nabla p + \nabla \cdot (vn \nabla \mathbf{v})$$

$$\partial_t(n\varepsilon) + \nabla \cdot (n\varepsilon\mathbf{v}) = -\nabla \cdot (nh(n, \varepsilon) \varepsilon\mathbf{u}) - p\nabla \cdot \mathbf{v} + \nabla \cdot (\lambda\nabla\varepsilon) + nv \nabla\mathbf{v}:\nabla\mathbf{v} \tag{21}$$
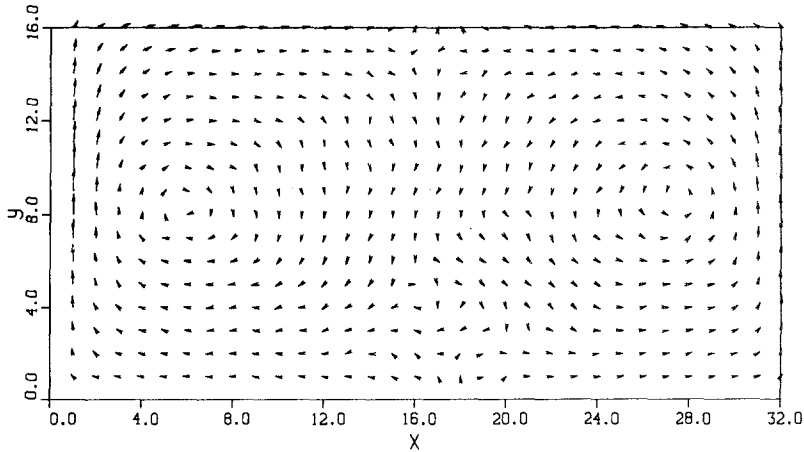
Fig. 14. Velocity vector distribution in Bénard convection. The bottom boundary has a temperature of 1.48 and the upper one has a temperature of 0.54. The left and right boundaries are adiabatic with a free-slip velocity condition being used for tangential velocity components.

The quantity h is the nonphysical additional term analogous to g in the momentum equation. For the Maxwell system,[50] h vanishes.

Numerical simulations of this temperature lattice gaas model have been done for several typical problems, including heat conduction and convection between two plates and Bénard instability problems. In Fig. 14, we present the velocity vector distributions in two-dimensional Bénard convection by chosing the lower boundary to have a higher temperature than the upper boundary. Typical vortices are seen. The simulation uses 512×256 lattices cells. The initial density and velocity loading are random. After about 30,000 times steps, we time average for 3000 steps. A spatial average of 16×16 cells is used to obtain macroscopic values. Then we can have 32×16 macroscopic cells. A nonslip condition for all walls and the adiabatic thermal condition for the left and right boundaries have been used. We have used different boundaries, such as a periodic condition for the lateral direction, keeping the upper and bottom boundaries as same as before. We also changed the wall to have nonslip conditions. All simulations show almost the same spatial velocity patterns.

6. MAGNETOHYDRODYNAMICS

The simple FHP lattice gas simulates a hard-sphere gas with zero radii. In order to obtain more interesting phenomena, such as two-phase

flows, phase transitions, and thermohydrodynamics, additional degrees of freedom are required, such as color, "bound pairs," and multiple speeds. These new properties of particles make it possible to extend the lattice gas to simulate different problems. Lattice gas methods can also be used to simulate magnetohydrodynamic (MHD) properties, as we describe below.

The incompressible MHD equations couple the velocity $\mathbf{v}$ and magnetic field $\mathbf{B}$. They can be written as follows:

$$\partial_t \mathbf{v} + \mathbf{v} \cdot \nabla \mathbf{v} = -\nabla p + (\nabla \times \mathbf{B}) \times \mathbf{B} + \nu \nabla^2 \mathbf{v}$$

$$\partial_t \mathbf{B} + \mathbf{v} \cdot \nabla \mathbf{B} = \mathbf{B} \cdot \nabla \mathbf{v} + \mu \nabla^2 \mathbf{B} \qquad (22)$$

$$\nabla \cdot \mathbf{v} = \nabla \cdot \mathbf{B} = 0$$

The magnetic vector potential $\mathbf{A}$ is related to $\mathbf{B}$ by $\nabla \times \mathbf{A} = \mathbf{B}$. The magnetic field modifies the motion of the fluid in the momentum equation through the Lorentz force $(\nabla \times \mathbf{B}) \times \mathbf{B}$. In two dimensions, $\mathbf{v}$ and $\mathbf{B}$ lie in the x–y space and depend on only those coordinates. We can choose the magnetic potential $\mathbf{A} = A\mathbf{z}$; the induction equation can then be replaced by a scalar equation for A,

$$\partial_t A + \mathbf{v} \cdot \nabla A = \nu \nabla^2 A \qquad (23)$$

Lattice gas automata models for MHD were first proposed by Montgomery and Doolen.[65,66] In their model, the scales quantity A is the fundamental variable and a magnetic potential "quantum number" $\sigma = 1, -1$, or 0 is assigned to each particle. Later, Chen et al.[16] introduced another lattice gas model for particles with two vectors and a "bidirectional" advection algorithm. The advantage of the latter approach is that all operations are purely local and no finite-difference operations on fluid fields are required to close the dynamical system. Each particle is labeled by two vectors, $\mathbf{e}_a$ and $\mathbf{e}_b (a, b = 1,..., 6)$. Therefore, for each lattice site, there are 36 states. No more than one particle in a lattice site can have the same (a, b). A particle has a defined momentum quantum $\mathbf{e}_a$ and a magnetic field quantum $\mathbf{e}_b$. The "bidirectional random walk" process in this model is performed as follows: during the advection process at each time step, a particle in state (a, b) will hop from one site to one of its six nearest neighboring sites either in the direction $\mathbf{e}_a$ with probability $1 - |P_{ab}|$, or in the direction $\text{sign}(P_{ab})\mathbf{e}_b$ with probability $|P_{ab}|$. The parameter P_{ab} $(|P_{ab}| \leqslant 1)$ is a function of (a, b) only. Let N_{ab} denote the particle occupation in the (a, b) state and define f_{ab} as the ensemble average of N_{ab}. Then the kinetic equation for f_{ab} is described by the following kinetic equation:

$$\partial_t f_{ab}(\mathbf{x}, t) + \{ 1 - |P_{ab}|) \mathbf{e}_a + P_{ab} \mathbf{e}_b \} \cdot \nabla f_{ab}(\mathbf{x}, t) = \Omega_{ab} \qquad (24)$$

where Ω_{ab} is again the collision operator, which is chosen to conserve the total mass, momentum, and magnetic field at each site.

The macroscopic number density n, momentum $n\mathbf{v}$, and magnetic field $\mathbf{B}$ are defined by

$$n = \sum_{a,b} f_{a,b}$$

$$n\mathbf{v} = \sum_{a,b} \{(1 - |P_{ab}|)\mathbf{e}_a + P_{ab}\mathbf{e}_b\} f_{ab} \tag{25}$$

$$n\mathbf{B} = \sum_{a,b} \{Q_{ab}\mathbf{e}_b + R_{ab}\mathbf{e}_a\} f_{ab}$$

The parameters P_{ab}, Q_{ab}, and R_{ab} are constant for a given system and are chosen in such a way that the moments of $(1 - |P_{ab}|)\mathbf{e}_a + P_{ab}\mathbf{e}_b$ and $Q_{ab}\mathbf{e}_b + R_{ab}\mathbf{e}_a$ will satisfy (22). Because the MHD system is invariant under proper or improper rotations, it can be shown that these parameters only need to depend on $|a - b|$. Because the velocity field is a vector field and B is pseudovector for 2D, the time evolution of the velocity field is unchanged if the magnetic field is reversed. This requires that $P_{ab} = -P_{ab+3}$, $Q_{ab} = Q_{ab+3}$, and $R_{ab} = -R_{ab+3}$. Hence, there are only six independent parameters in this model. These are chosen to be P_{aa}, P_{aa+1}, Q_{aa}, Q_{aa+1}, R_{aa}, and R_{aa+1}.

Using a Chapman–Enskog expansion for low Mach number, one can show that n, $\mathbf{v}$, and $\mathbf{B}$ approximately obey the following equations:

$$\partial_t n + \nabla \cdot (n\mathbf{v}) = 0$$

$$\partial_t(n\mathbf{v}) + \nabla\left[C_1 \frac{n}{6} - \frac{1}{2} ng(n)(C_2\mathbf{v}^2 - C_3\mathbf{B}^2)\right]$$

$$= -\nabla \cdot ng(n)[C_2\mathbf{vv} - C_3\mathbf{BB}] + \nu\nabla^2(n\mathbf{v}) \tag{26}$$

$$\partial_t(n\mathbf{B}) + (D_1 - D_3)\nabla \cdot [ng(n)\,\mathbf{Bv}] + (D_2 + D_3)\nabla \cdot [ng(n)\,\mathbf{vB}]$$

$$= D_3\,\nabla[ng(n)\mathbf{v} \cdot \mathbf{B}] + \mu\nabla^2(n\mathbf{B})$$

where $g(n) = (n - 18)/(n - 36)$. The detailed expressions of the coefficients C_1, C_2, C_3, D_1, D_2, D_3, ν, and μ only depend on the six free parameters.[16] By properly selecting the values of the six parameters subject to the conditions $C_2 = D_1 = D_2 \geqslant 0$, $D_3 = 0$, and $C_1 \geqslant 0$, together with the rescaling of the time by the $g(n)$ factor, the MHD equations (22) are obtained in the low-Mach-number limit.

Assume that $\mathbf{B} = \mathbf{B}_0 + \delta\mathbf{B}$ and $\mathbf{v} = \delta\mathbf{v}$, where $\mathbf{B}_0 = B_0\mathbf{e}_y$, B_0 is constant,

and $\mathbf{e}_y$ is the unit vector in the y direction; the linearization of Eq. (26) gives the following wave equation for $\delta\mathbf{B}$:

$$\frac{\partial\delta\mathbf{B}}{\partial t} = (\mathbf{B}_0 \cdot \nabla)\,\delta\mathbf{v}$$

$$\mu\rho\,\frac{\partial(\delta\mathbf{v})}{\partial t} = (\mathbf{B}_0 \cdot \nabla)\,\delta\mathbf{B} \tag{27}$$

It is easy to get the wave propagation speed a (Alfvén wave speed):

$$a = \frac{B_0}{(\mu n)^{1/2}}$$

In Fig. 15, we show the simulation results for Alfvén wave speed compared with analytical results for density 0.1 and 0.3. The simulation has been done for a system with 8192×128 lattice cells. The wave speed is measured by the correlation functions in the long-wave limit.[18]

Hartman flow is a two-dimensional (in the x–y plane) steady channel flow with conducting and nonslip boundaries on the two walls with a distance $2L$; the flow is driven by the pressure difference between two edges along the x direction while keeping the y-direction magnetic field to be
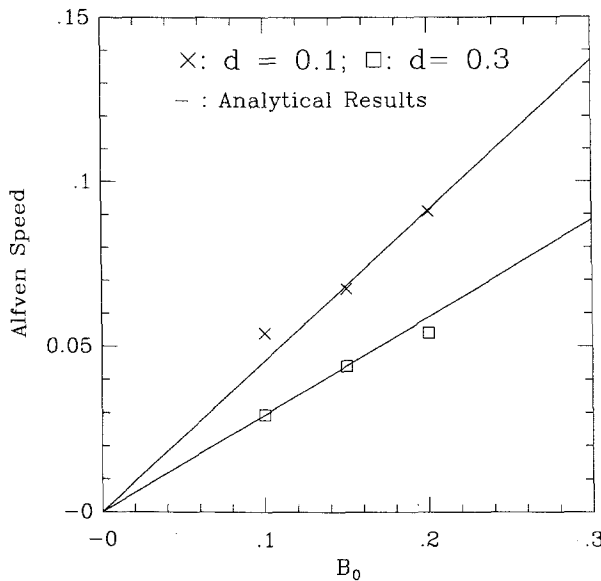

Fig. 15.   Afvén wave speed versus the magnetic intensity B_0 for density $d = 0.1$ and $d = 0.3$.
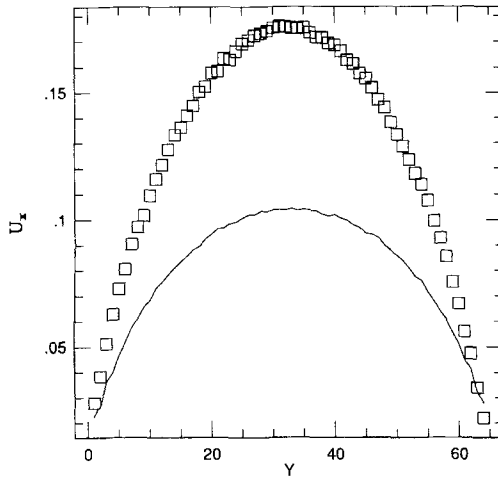The solid lines are the analytical results.

Fig. 16. The x-direction velocity distribution across the channel for a Hartman flow. The solid line is the case with $B_y = 0.1$ and the squares represent the case with $B_y = 0$.

constant everywhere. There are two kinds of boundaries for B_x on the walls: (i) $\partial_y B_x = 0$; (ii) $B_x = $ const. Here we only show the first case. In the lattice gas simulation, we use a homogeneous forcing along the flow direction to replace the pressure difference. The forcing only changes the momentum along the flow direction by flipping particles in the negative flow direction to the positive flow direction with a given probabililty. There
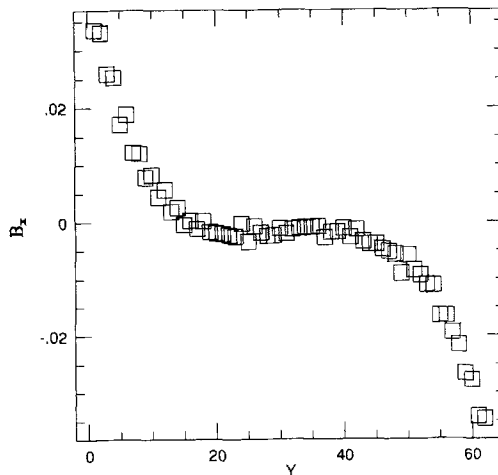

Fig. 17. The x-direction magnetic field distribution across the channel with $B_y = 0.1$, seen to be an odd function of y in accordance with the exact solutions.

are no B changes during the forcing processes. The constant B_y is controlled by a periodic condition in the y direction. In order to have $\partial_y B_x = 0$ on $y = 0$ and $2L$ and satisfy the odd-function requirement for B_x, the simulation has used a channel with of $4L$: the forcing from $y = 0$ to $y = 2L$ is along the positive x direction, while the forcing in another half-space is along the negative x direction. This forcing will give the zero-velocity condition for $y = 0$ and $2L$. Because all quantities are only functions of y, we use a periodic condition for the x direction and all physical quantities are averaged along the x direction. In Fig. 16, we present the typical velocity distribution for Hartman number $H = 2$ (the solid line) compared with $H = 0$ ($\square$) when they have the same magnitude of forcing, where H is defined as $H = B_y L/(\mu v)^{1/2}$, where μ and v are the resistivity and kinematic viscosity, respectively. We clearly see the departure of the velocity from a parabolic distribution for the zero magnetic field case. In Fig. 17, we show B_x as a function of the channel width; it can be seen that this lattice gas model preserve the odd-function feature of the B_x field.

7. CONCLUDING REMARKS

In this paper, we have discussed several lattice gas models which are capable of qualitatively reproducing important physical features.

From a theoretical point of view, it would be interesting to have a lattice gas model with the Galilean-invariance property, for which the convective coefficient g is unity for all densities. This is also a crucial requirement for simulating compressible high-Mach-number flows. Multi-speed lattice gas models provide one possibility for overcoming this problem,[20,29,43,63] but most method usually are only good either for a single density or for small density variation.

In order to simulate high-Reynolds-number flows,[67] it is essential to increase the Reynolds number. Recent studies have achieved some success by violating the semi-detailed belance condition[37,75] for collision operators. But this scheme usually lacks rigorous theoretical fundations, in cluding the form of the equilibrium dfistribution. How to prove the generalized H-theorem for such a system and derive the kinetic theory are still open.[56]

Even though the lattice gas methods have been used for diverse dynamic systems, it seems that this method still has potential applications to many new fields, which may include some complicated physical phenomena, such as chemical reacting flows, non-Newtonian fluids, and solidification, for which the particle picture is the natural description.

ACKNOWLEDGMENTS

REFERENCES

1. K. Balasubramanian, F. Hayot, and W. F. Saam, *Phys. Rev. A* **36**:2248–2253 (1987).
2. D. Bernardin, O. E. Sero-Guillaum, and C. Sun, Multispecies 2D lattice gas with energy levels: Diffusive properties, *Physica D* (1990), in press.
3. P. M. Binder, *Complex System* **3**:1–7 (1989).
4. P. M. Binder and D. d'Humières, *Phys. Lett. A* **140**:465–468 (1989).
5. B. M. Boghosian and C. D. Levermore, *Complex Systems* **1**:481–496 (1987).
6. J. U. Brackbill, D. B. Kothe, and C. Zemach, A continuum method for modeling surface tension, preprint (1990).
7. U. Brosa, C. Huettner, and U. Werner, Flow through a porouos membrane simulated by cellular automata and by finite elements, *J. Stat. Phys.* (1990).
8. J. E. Broadwell, *Phys. Fluids* **7**:1243–1247 (1964).
9. D. Burgess, F. Hayot, and W. F. Saam, *Phys. Rev. A* **38**:3589–3592 (1988).
10. C. Burges and S. Zaleski, *Complex Systems* **1**:31–50 (1987).
11. H. Cabannes and D. H. Tiem, *Complex System* **1**:575–584 (1987).
12. A. Cécile and S. Zaleski, *Phys. Rev. Lett.* **64**:1 (1990).
13. A. Cecile, D. H. Rothman, and S. Zaleski, A liquid–gas model on a lattice, *Physica D* (1990), in press.
14. H. Chen, S. Chen, G. D. Doolen, Y. C. Lee, and H. A. Rose, *Phys. Rev. A* **40**:2950–2853 (1989).
15. H. Chen, S. Chen, G. D. Doolen, and Y. C. Lee, *Complex Systems* **2**:259–267 (1988).
16. H. Chen, W. H. Matthaeus, and L. W. Klein, *Phys. Fluids* **31**:1439–1445 (1988).
17. H. Chen, W. H. Matthaeus, and L. W. Klein, *J. Comput. Phys.* **88**:433 (1990).
18. S. Chen, H. Chen, G. D. Doolen, Y. C. Lee, H. Rose, and H. Brand, Lattice gas models for nonideal gas fluids, *Physica D* **47**:97 (1991).
19. S. Chen, K. Diemer, G. D. Doolen, K. Eggert, S. Gutman, and B. J. Travis, Lattice gas automata for flow through porous media, *Physica D* **47**:72 (1991).
20. S. Chen, Hudong Chen, Gary D. Doolen, Semion Gutman, and Minxu Lee, A lattice gas model for thermohydrodynamics, *J. Stat. Phys.* **62**:1121 (1991).
21. S. Chen, G. D. Doolen, K. Eggert, D. Grunau, and E. Y. Loh, A local lattice gas model for immiscible fluids, *Phys. Rev. A* **43**:245 (1991).
22. S. Chen, Zhen-su She, L. C. Harrison, and Gary D. Doolen, *Phys. Rev. A* **39**:2725–2727 (1989).
23. Z. Chen, J. L. Lebowitz, and E. R. Speer, Microscopic shock structure in model particle systems: The Boghosian–Levermore cellular automata revisited, preprint (1990).
24. B. Chopard and M. Droz, *Phys. Lett. A* **126**:476–480 (1988).
25. P. Clavin, D. d'Humières, Y. Pomeau, and G. Searby, *J. Fluid. Mech.* **188**:437–464 (1988).
26. R. Cornubert, D. d'Humières, and D. Levermore, A Knudsen layer theory for lattice gases, *Physica D* (1990), in press.

27. D. Dab and J.-P. Boon, Cellular automata approach to reaction–diffusion systems, in *Cellular Automata and Modeling of Complex Physical Systems*, P. Manneville, N. Boccara, G. Y. Vichniac, and R. Bidaux, eds. (Springer-Verlag, 1989), pp. 257–273.
28. J. P. Dahlburg, D. Montgomery, and G. D. Doolen, *Phys. Rev. A* **36**:2471–2474 (1987).
29. D. d'Humières, P. Lallemand, and G. Searby, *Complex Systems* **1**:333–350 (1987).
30. K. Dimer, K. Condie, S. Chen, T. Shimomura, and G. Doolen, Density and velocity dependence of Reynolds numbers for several lattice gas models, in *Lattice Gas Automata for Partial Differential Equations*, Gary D. Doolen, ed. (Addison-Wesley, 1989), pp. 137–178.
31. D. d'Humières, P. Lallemand, and U. Frisch, *Europhys. Let.* **2**:291 297 (1986).
32. F. A. L. Dullien, *Porous Media, Fluid Transport and Pore Structure* (Academic Press, 1979).
33. G. D. Doolen, ed., *Complex Systems* **1**(4):545–851 (1987).
34. G. D. Doolen, ed., *Lattice Gas Methods for PDEs* (Addison-Wesley, 1989).
35. G. D. Doolen, ed., Lattice gas methods for PDE's: Theory, applications and hardware, *Physica D*, in press.
36. M. Droz and B. Chopard, Non-equilibrium phase-transitions and cellular automata, *Chaos and Complexity*, R. Lovi, S. Roffo, S. Ciliberto, and M. Buiatti, eds. (World Scientific, 1988), pp. 307–317.
37. B. Dubrulle, *Complex Systems* **2**:577–609 (1988).
38. M. H. Ernst, Mode-coupling theory and tails in CA-fluids, *Physica D* (1990), in press.
39. M. H. Ernst and J. W. Duffy, *J. Stat. Phys.* **58**:57–86 (1990).
40. D. Frenkel and M. H. Ernst, *Phys. Rev. Lett.* **63**:2165–2168 (1989).
41. U. Frisch, B. Hasslacher, and Y. Pomeau, *Phys. Rev. Lett.* **56**:1505 (1986).
42. U. Frisch, D. d'Humières, B. Hasslacher, P. Lallemand, Y. Pomeau, and J.-P. Rivet, *Complex Systems* **1**:649–707 (1987).
43. A. K. Gunstensen and D. Rothman, A Galilean-invariant immiscible lattice gas, *Physica D* (1990), in press.
44. J. Hardy, O. de Pazzis, and Y. Pomeau, *Phys. Rev. A* **13**:1949–1961 (1976).
45. J. Hardy and Y. Pomeau, *J. Math. Phys.* **13**:1042–1051 (1972).
46. B. Hasslacher, *Los Alamos Sciences* **15**:211–217 (1988).
47. F. Hayot, Fingering instability in a lattice gas, *Physica D* (1990), in press.
48. M. Henon, *Complex Systems* **1**:179–208 (1987).
49. J.-I. Huang, Y.-H. Chu, and C.-S. Yin, *Geophys. Res. Lett.* **15**:1239–1241 (1988).
50. K. Huang, *Statistical Mechanics* (Wiley, New York, 1987).
51. L. Kadanoff, G. McNamara, and G. Zanetti, *Phys. Rev. A* **40**:4527–4541 (1989).
52. X. P. Kong and E. G. D. Cohen, A kinetic theorist's look at lattice gas cellular automata, *Physica D* (1990), in press.
53. M. Kosterlitz and D. J. Thouless, *J. Phys. C* **6**:1181 (1973).
54. A. Ladd, E. Michael, and A. Frankel, *Phys. Rev. Lett.* **60**:975–978 (1988).
55. A. Lawniczak, D. Dab, R. Kapral, and J.-P. Boon, Reactive-lattice gas automata, *Physica D* (1990), in press.
56. D. Levermore, Private communication.
57. E. Y. Loh, S. Chen, and G. D. Doolen, Two-dimensional high Reynolds number simulations on the CM-2, preprint.
58. L. S. Luo, H. Chen, S. Chen, G. Doolen, and Y. C. Lee, Generalized hydrodynamic transport in lattice gas automata, *Phys. Rev. A* **43**:536 (1991).
59. F. Liu and N. Goldenfeld, Deterministic lattice gas model for diffusion-controlled crystal growth, *Physica D* (1990), in press.
60. A. Majda, *Compressible Fluid and Systems of Conservation Laws in Several Space Variables* (Springer-Verlag, 1984).

61. G. R. McNamara and G. Zanetti, *Phys. Rev. Lett.* **61**:2332–2335 (1988).
62. N. Metropolis *et al.*, *J. Chem. Phys.* **21**:1087 (1953).
63. K. Molvig, P. Donis, J. Myczkowski, and G. Vichniac, Continuum fluid dynamics from lattice gas, MIT (1988), preprint.
64. R. Monaco, ed., *Discrete Kinetic Theory, Lattice Gas Dynamics and Foundations of Hydrodynamics* (World scientific, 1989).
65. D. Montgomery and G. D. Doolen, *Phys. Lett. A* **120**:229–231 (1987).
66. D. Montgomery and G. D. Doolen, *Complex Systems* **1**:831–838 (1987).
67. S. A. Orszag and V. Yakhot, *Phys. Rev. Lett.* **56**:1691–1693 (1986).
68. Y. H. Qian, D. d'Humières, and P. Lallemand, Diffusion simulation with a deterministic one-dimensional lattice gas models, ENS (1989), preprint.
69. K. I. Read, *Physica D* **12**:45–48 (1984).
70. M. Rieger and P. Vogel, *Solid State Electronics* **32**:1399–1403 (1989).
71. J.-P. Rivet, M. Henon, U. Frisch, and D. d'Humières, *Europhys. Lett.* **7**:231–236 (1988).
72. D. H. Rothman, *Geophysics* **53**:509–518 (1988).
73. D. H. Rothman and J. M. Keller, *J. Stat. Phys.* **52**:1119–1127 (1988).
74. D. H. Rothman and S. Zaleski, *J. Phys.* (Paris) **50**:2161–2174 (1989).
75. D. H. Rothman, *J. Stat. Phys.* **56**:1119–1127 (1989).
76. G. Searby, V. Zahnle, and B. Denet, Lattice gas mixture and reactive flows, in *Discrete Kinetic Theory, Lattice Gas Dynamics and Foundations of Hydrodynamics*, R. Monaco, ed. (World Scientific, 1989), pp. 300–314.
77. T. Shimomura, G. D. Doolen, B. Hasslacher, and C. Fu, *Los Alamos Science Special Issue* **1987**:201–210 (1987).
78. J. A. Somers and P. E. Rem, Analysis of surface tension in two-phase lattice gas, *Physica D* (1990), in press.
79. J. P. Straley, *Phys. Rev. A* **4**:675 (1985).
80. S. Succi, C. Chang, E. Foti, M. Gramignami, and D. Rothman, A direct computation of the permeability of three-dimensional porous media, in International Conference on Numerical Methods in Groundwater Resources (1990), to be published in Comp. Mec. Institute.
81. S. Succi, P. Santangelo, and R. Benzi, *Phys. Rev. Lett.* **60**:2738–2741 (1988).
82. S. Wolfram, *J. Stat. Phys.* **45**:19–74 (1986).
83. G. Zanetti, *Phys. Rev. A* **403**:1539–1548 (1989).